nature communications

Article

https://doi.org/10.1038/s41467-026-70295-5

An equilibrium rotator glass-forming phase for long-ranged repulsive colloidal rods

Received: 28 February 2025

Accepted: 24 February 2026

Published online: 18 March 2026

Check for updates

Thijs Herman Besseling [1,2] ✉, Berend van der Meer[1,3], Bing Liu [1,4], Laura Filion[1], Arnout Imhof [1] & Alfons van Blaaderen [1] ✉

Glasses, amorphous solid phases nearly always out of equilibrium, remain poorly understood despite recent progress. Here we show by quantitative real-space experiments and computer simulations the existence of an equilibrium glass-forming phase which forms due to a subtle interplay between the rotational and translational degrees of freedom in a system of charged colloidal rods. In this rotational glass-forming phase, the positional coordinates are glass-like, while the rotations remain liquid-like. This phase can be reversibly switched into a crystalline solid through a first-order phase transition with minimal particle rearrangements by an external electric field. We speculate that this rotator glass-like phase forms due to the anisotropic particle interactions at higher volume fractions, destabilizing the crystal. Finding an equilibrium glassy rotator phase will lead to new insights on how translations and rotations affect phase behavior, including glass formation and, additionally, allow new theoretical approaches to be used to study the glass transition.

The important differences in the properties between liquids and crystalline solids can be explained by differences in both their structure and dynamics. In terms of structure, particles in liquids have short-ranged positional and orientational order, while for crystals both are long-ranged[1]. With respect to the dynamics, in crystals the long-time self-diffusion coefficients for both translations and rotations of particles are typically zero on experimental time scales, while in liquids both display significant mobility. Additional states of matter are possible—often associated with anisotropic shaped particles or molecules, like rods or plates—where some of the degrees of freedom associated with either the positional or orientational order and dynamics are like those of crystals, while the remaining degrees of freedom behave like those of liquids[1–3]. Such phases have interesting mixes of properties. For instance, in rotator crystals some or all of the rotational degrees of freedom are liquid-like, while the positional order is that of a solid[2,4]. The rotations of the molecules weaken the strength of such solids so much that they can deform under their own weight, leading to the name "plastic crystals"[2]. On the other hand, phases where (some of) the rotational degrees of freedom are solid-like, but the positional coordinates have the dynamics of liquids can flow and hence are called liquid crystals[3,5]. The ability of such phases to rotate the polarization of light is used in nematic liquid crystals displays[6].

Glasses are yet another important and intriguing class of materials: they are solids whose structure resembles that of a liquid, but where the particles' long-time self-diffusion coefficients are as small as for crystals[7–18]. They are often described as liquids that have solidified before their structure becomes crystalline and thus are out of equilibrium[7–13]. However, not all non-crystalline solids are inherently out of equilibrium. For example, particles that can form a small number of flexible bonds with their neighbors can form an arrested disordered equilibrium state at low temperatures[19,20], although for different reasons than the phase discussed in the present work.

In this work, we demonstrate the existence of an equilibrium rotator glass-like phase. This phase exhibits two intriguing properties: a combination of liquid-like rotations and translational dynamics which are near dynamical arrest, as well as being an equilibrium phase with short-ranged positional order. We explore this phase using both

[1]Soft Condensed Matter and Biophysics, Debye Institute for Nanomaterials Science, Utrecht University, Utrecht, The Netherlands. [2]Present address: Imec at Holst Centre, Eindhoven, The Netherlands. [3]Present address: Physical Chemistry and Soft Matter, Wageningen University and Research, Wageningen, The Netherlands. [4]Present address: Beijing National Laboratory for Molecular Sciences, Institute of Chemistry, Chinese Academy of Sciences, Beijing, China. ✉e-mail: t.h.besseling@uu.nl; a.vanblaaderen@uu.nl

real-space experiments on charged colloidal rod-shaped particles[4,5,21,22] and computer simulations.

Results

We studied a system of fluorescently labeled, micron-sized, charged silica rods with a shape resembling spherocylinders[4,5,21,22] characterized by an end-to-end length l, diameter d and aspect ratio l/d ~ 4 (Fig. 1a). The rods were dispersed in an index matching solvent which reduces the van der Waals attractions to values small compared to the thermal energy k_BT. Additionally, the particles were coated with short ligand molecules which provide them with a repulsive interaction that is steep and short-ranged with respect to the rod diameter and length. Finally, the range of the charge-based repulsions is characterized by the Debye screening length κ^{-1}, which is directly related to the ionic strength of the suspending fluid. When the ionic strength is relatively large and hence κ^{-1} is short (Fig. 1b), the particles form the phases known for hard rods, which for $l/d > 3.5$ are smectic LC phases[3,5,22]. These are 1D solids, with 2D liquid layers of parallel oriented rods (Figs. 1c,d). Conversely, at low ionic strength, the repulsions are dominant over the particle shape and when κ^{-1} becomes comparable to l (Fig. 1e) rotator crystal (or plastic crystal) phases can be formed[4]. Figure. 1f,g shows an example of a body-centered-cubic (BCC) plastic crystal (viewed from BCC(110) plane). For $\kappa l = 0.8$, i.e., at a screening length similar to the particle length, the rods still form a rotator crystal phase at intermediate densities. However, when the rods were compressed to high enough densities, the system failed to crystallize, and instead formed a 'rotator glassy phase' (Fig. 1i,j). This phase lacks long-ranged positional order, highlighted by the FFT in the inset Fig. 1j. Additionally, in this

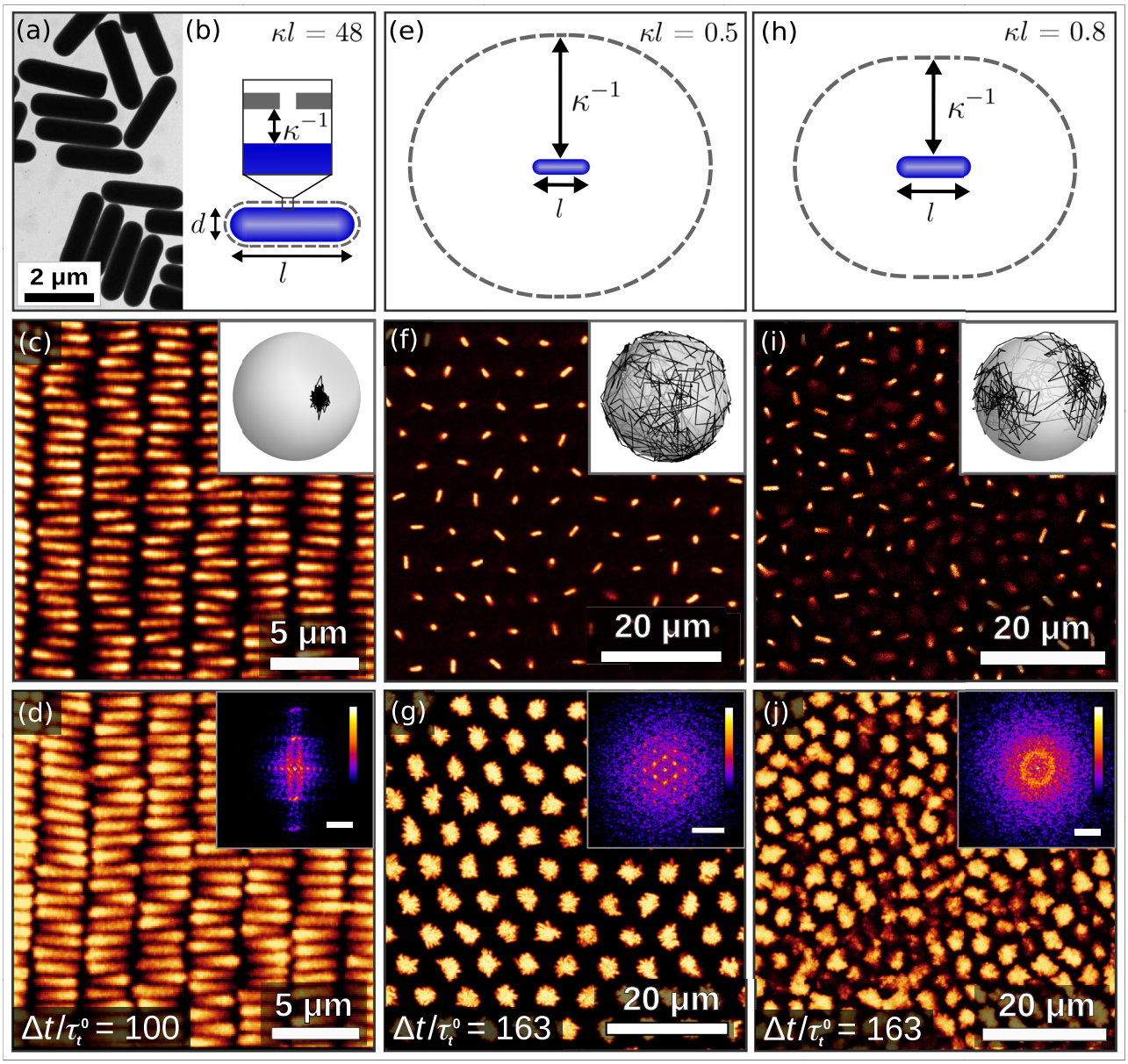

Fig. 1 | Phase behavior of fluorescent silica rods with fixed aspect ratio but varying screening length and number density. a TEM micrograph of silica rods with average end-to-end length $l = 2.4\ \mu$m, diameter $d = 640$ nm, and aspect ratio $l/d = 3.8$. **b**, **e**, **h** Schematics showing how the screening length κ^{-1} changes the effective dimensions of the particle. **c**, **f**, **i** Single confocal microscopy images. The insets show a typical rotational trajectory of a single particle on the unit sphere obtained from 3D particle tracking. **d**, **g**, **j** Superposition of multiple confocal microscopy images over a time window indicated in the image. The insets show a 2D FFT of the monochrome confocal microscopy images. The color bar indicates a logarithmic intensity scale. The scale bar in the inset in (**d**) indicates 9 μm^{-1}, and in (g,j) 3 μm^{-1}. **b**–**d** For $\kappa l = 48$, rods form a liquid crystalline smectic-B phase. **e**–**g** For $\kappa l = 0.5$ and $\phi = 0.005$, particles form a plastic (or rotator) crystal. **h**–**j** For $\kappa l = 0.8$ and ϕ ~0.02, particles form a rotator glassy phase.

https://doi.org/10.1038/s41467-026-70295-5

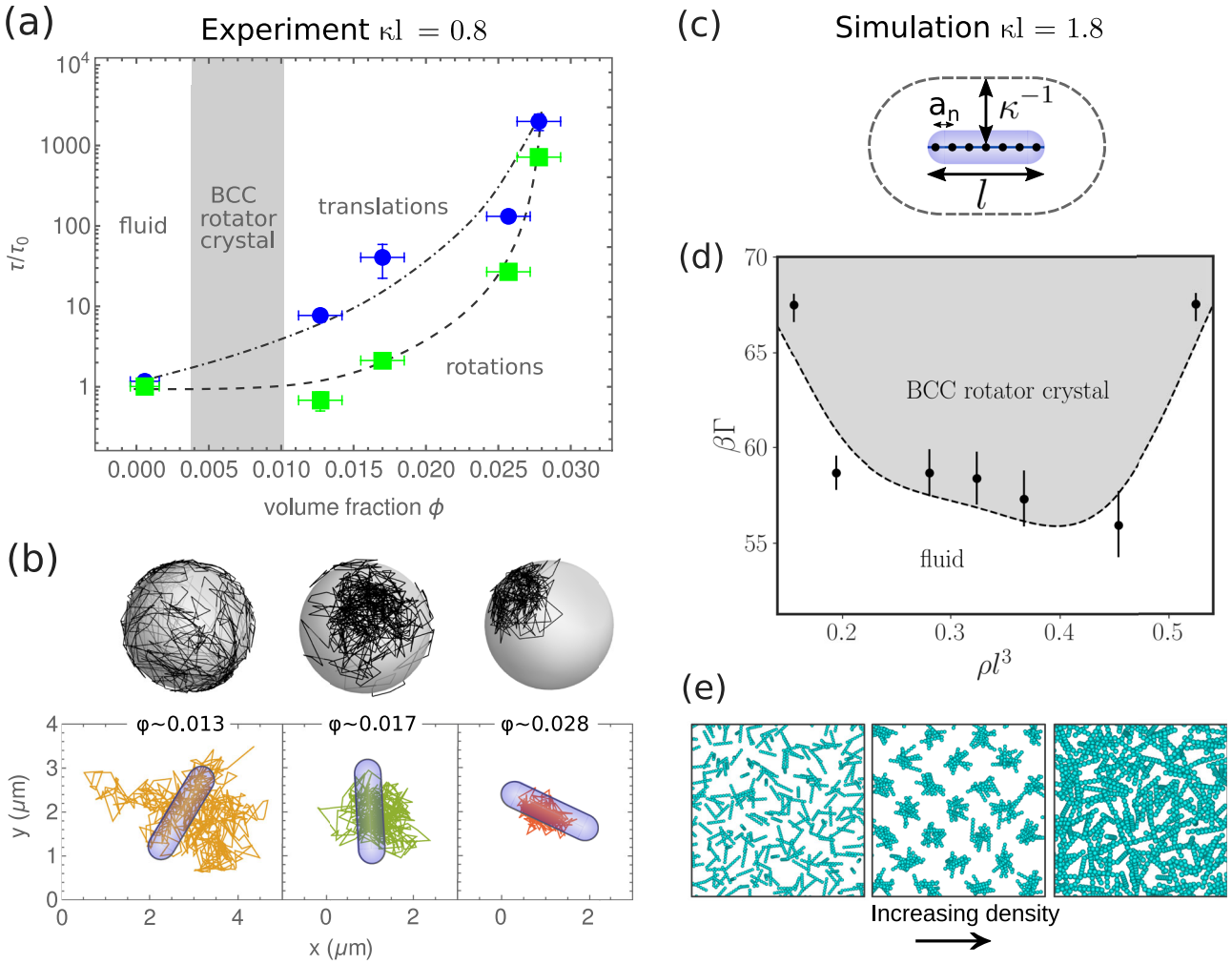

Fig. 2 | Equilibrium phase transitions from a dense fluid to a glassy rotator phase. a Rotational and translational relaxation times of amorphous phases as function of volume fraction ϕ, for an experimental system with $\kappa l = 0.8$. Lines are drawn to guide the eye only. The light gray area on the left indicates the region where the BCC rotator crystal was stable. The error bars represent the standard deviation. **b** Typical 3D rotational and translational trajectories of a particle for increasing volume fraction. **c** Yukawa segment model used in the simulation with $\kappa l = 1.8$ and $n = 7$. A spherocylinder with the same aspect ratio as in the experiments is drawn around the segment-model for visualization purpose. **d** Phase diagram obtained from simulation showing the stability of a re-entrant fluid phase at higher particle concentrations. **e** Simulation snapshots of three phases resembling the phases of the experimental system shown in Supplementary Fig. 1.

phase the particles are strongly caged by their neighbors, leading to glass-like translational motion, whereas rotational motion remained almost free. This is shown in Fig. 1j by the superposition of 500 images, measured over a time-interval $\Delta t = 163\,\tau_t^0$, with τ_t^0 the time for the rod to diffuse over its own diameter at infinite dilution.

To get a more quantitative picture of the dynamics of this phase, we analyzed particle trajectories from 3D confocal microscopy image-stacks as a function of increasing volume fraction ϕ (see Supplementary Fig. 1 and Supplementary Mov. 1), and calculated the translational and rotational self-correlation functions and analyzed the resulting relaxation times (for details see the Methods section and Supplementary Fig. 2) as well as the mean-squared displacements (Supplementary Fig. 3a,b). Figure 2a demonstrates that for a volume fraction of $\phi \approx 0.017$, the translational diffusion slowed down by two orders of magnitude, while the rotational diffusion remained much more constant. At this volume fraction, particle trajectories were almost completely caged for the duration of the experiment (see Fig. 2 b for a typical particle trajectory and Supplementary Fig. 3c for a larger ensemble) while we also clearly observed dynamical heterogeneities (see Supplementary Fig. 4), a hallmark of a system approaching the glass transition[23]. At the highest volume fraction we investigated ($\phi > 0.020$), rotations also started to freeze in (Fig. 2a–b).

To explore the origin of this rotator glass-like phase, we performed computer simulations and free-energy calculations on a simplified model for charged colloidal rods. To this end, we employed a Yukawa segment model[24], in which a charged rod is divided into in n segments of equally distributed point charges along the rod axis, see Fig. 2c. The interactions between two rods is then given by the sum of the interactions between the segments, see Methods. Note that in the model system the interactions are significantly shorter-ranged ($\kappa l = 1.8$) than in the experiments to make the simulations more feasible. Specifically, this choice ensures all our simulations needed to probe the phase diagram are either fluid or crystal, and hence can be equilibrated without issue. The equilibrium phase behavior of these soft rod-like particles was determined by calculating the Helmholtz free energy of both the fluid phase and the BCC rotator crystal phase, as described in the Methods. The phase diagram is shown in Fig. 2d. In agreement with experiments, we find that for sufficiently charged rods (high enough Γ), the system undergoes a fluid to a BCC rotator crystal phase transition at intermediate densities followed by a re-entrant BCC rotator crystal to fluid transition at higher densities. Hence, these free-energy calculations clearly suggest a thermodynamic origin for a re-entrant disordered phase in the less long-ranged and approximated computer simulations model. The re-entrant stability of the disordered phase can

https://doi.org/10.1038/s41467-026-70295-5

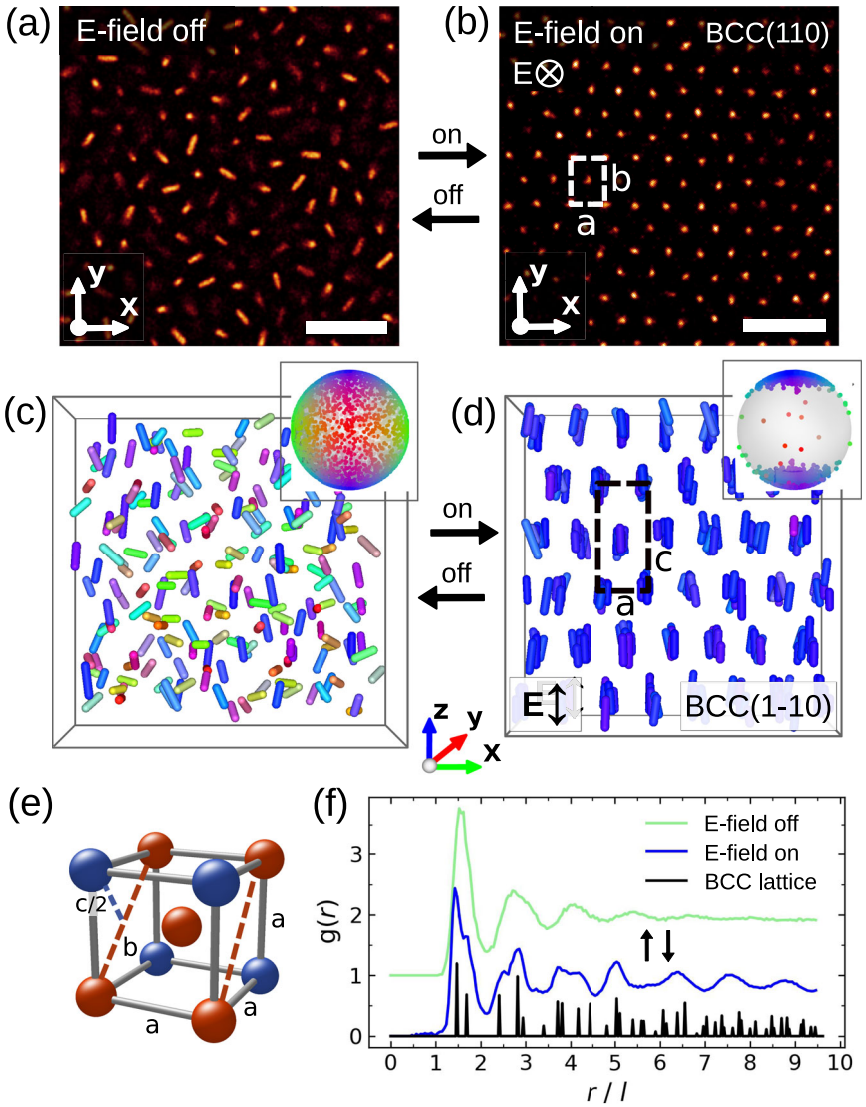

Fig. 3 | Reversible crystallization and melting by AC electric-field induced particle alignment. a, **b** Crystallization of the plastic glassy phase induced by applying a high-frequency AC electric field (E = 90 V/mm) and subsequent melting when the field was turned off (κl = 0.8 and ϕ ~0.02). Scale-bars are 10 μm. **c**, **d** 3D reconstruction of a rotator glass-former and BCC crystalline phase, obtained from 3D confocal microscopy data. Particles are color-coded according to their orientation. **d** View from the BCC(1-10) plane. The BCC lattice is approximately 33% streched in the field (z) direction. **e** BCC unit cell. **f** 3D radial distribution functions g(r). The green line corresponds to the rotator glass-forming phase (with no field applied) and is shifted upwards for clarity. The blue line is for a crystalline phase formed under application of an electric field.

be explained by the frustrations induced by the effective correlated orientations the particles undergo as the system is compressed. At low and intermediate densities, the particles are far apart due to the charge repulsion, and as a result the interactions are more isotropic. In contrast, at higher densities, the closer proximity of particles to their neighbors implies that the shape of the particle plays an important role in the interactions. As a result, different pairs of particles feel effectively different interactions based on their orientations, causing an effective polydispersity in the interactions. This would lead to frustration, a well known driver of glass formation[12,25].

To investigate the dynamics of this re-entrant disordered phase, we performed Brownian dynamics simulations of the Yukawa segment model[26]. We calculated the mean square displacement $\langle \Delta r^2(t) \rangle$ for a wide range of densities ρ and extracted the long-time translational diffusion coefficient D_t, which we rendered dimensionless by normalization with D_t^0 (Supplementary Fig. 5). At sufficiently high densities, the diffusivity decreased exponentially with increasing density. This highlights, as expected, a gradual arrest of the dynamics as the density is increased. Although in the model system the interactions are significantly shorter-ranged, there is good qualitative agreement between simulation and experiment (compare also Fig. 2e with Supplementary Fig. 1).

To further illustrate experimentally the thermodynamic origin and nature of the phase near dynamical arrest, we applied an external high-frequency AC electric field that aligned the particles with the field direction. We show in Fig. 3 (see also Supplementary Fig. 6 and Supplementary Mov. 2,3) that subsequently the rotator glass-like phase transformed into a 3D crystal. The field restricted the rotations of the rods, and as a result it lowered the anisotropy of the particle interactions allowing them to form a BCC lattice stretched in the field direction (see also Supplementary Fig. 7). Once the electric field was turned off, particles regained their orientational freedom and the crystalline phase reverted back to a rotator glassy phase, which demonstrates that this glass-forming amorphous phase has a lower free energy than the crystalline phase. The radial distribution function $g(r)$ (Fig. 3f) shows the lack of long-ranged order in the near-arrested rotator phase.

https://doi.org/10.1038/s41467-026-70295-5

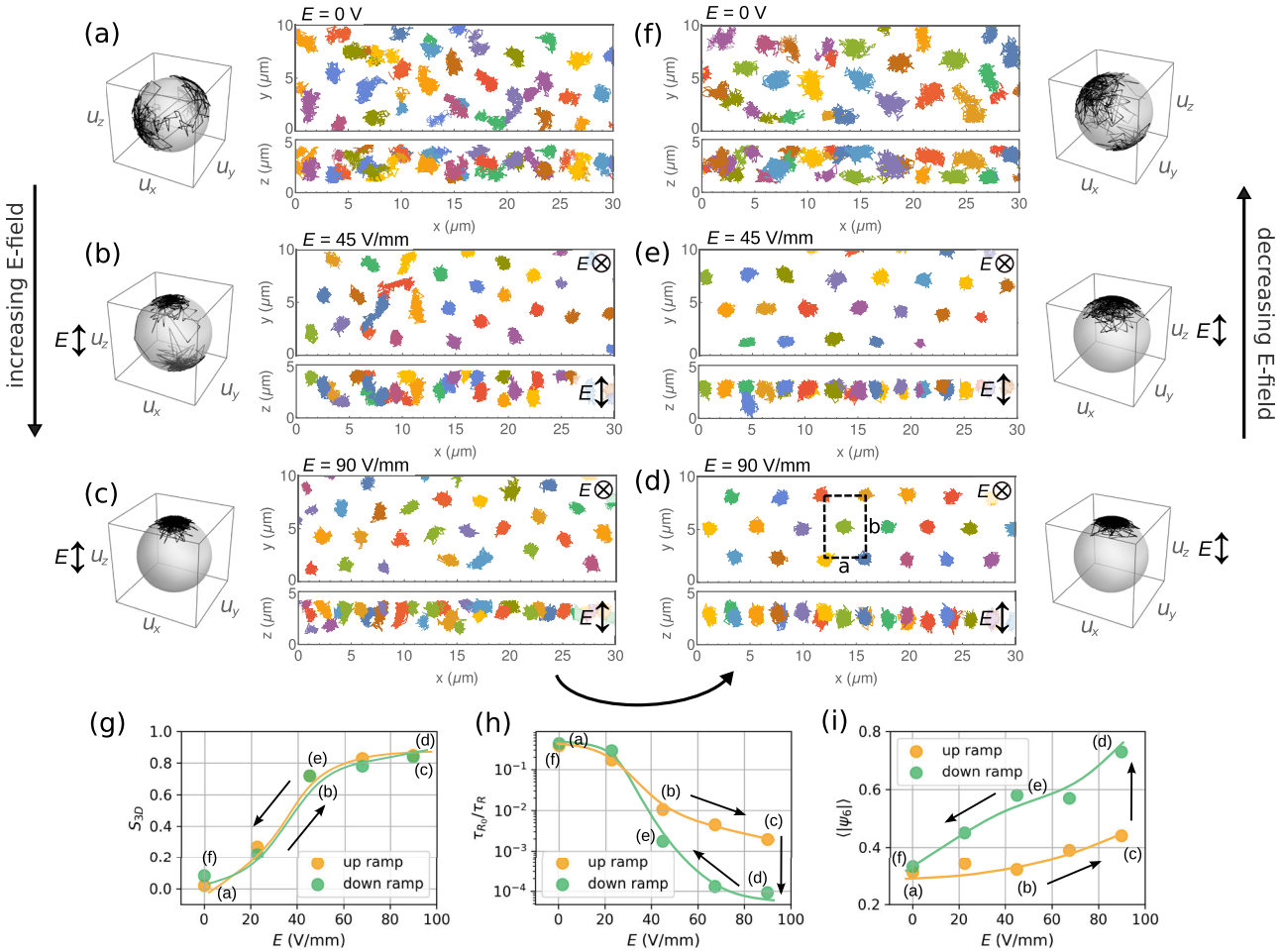

Fig. 4 | Hysteresis of positional order during a reversible transition between a rotator glass-forming phase and a crystalline phase. The transitions were induced by slowly increasing and decreasing the electric-field strength. The duration of each measurement was 141 s and the time interval between measurements was 4 min, $\kappa l = 0.8$ and ϕ ~0.02. **a**–**f** Shown are x-y projections of the 3D translational trajectories together with a typical rotational trajectory of a single particle. **a**–**c** Upon increasing the electric field strength, particles in a rotator glassy phase first align with the field and subsequently formed ordered domains. Between (**c**) and (**d**), the sample was left to equilibrate for 1 h under a constant E-field of 90 V/mm after which the sample became fully crystalline. **d**–**e** Upon decreasing the electric field again, crystalline order still persisted. **f** At zero field strength, the system relaxed back to the amorphous glass-like phase. **g** 3D nematic order parameter S_{3D}, (**h**) normalized rotational relaxation time τ_0/τ_R and (**i**) average local hexagonal bond-order parameter $\langle|\psi_6|\rangle$ as a function of E-field strength.

We studied the reversibility of the rotator glassy phase to crystal transition by changing the electric field strength in smaller and slower steps. As shown in Fig. 4, we observed strong hysteresis effects, indicative of a first-order phase transition. Particles quickly aligned and then started to order positionally more slowly (Fig. 4a–c). The sample initially became polycrystalline over larger distances (~ 100 μm), but after approximately 1 h large ordered domains were present (Fig. 4d). When the field strength was then decreased again, strong hysteresis was observed in both the rotational dynamics and positional order (Fig. 4h–i). When the field strength dropped below approximately E = 45 V/mm, the (rotator) crystalline lattice became unstable, and completely returned to the original rotator glass-like state. When the electric field was increased and decreased at much faster rates (Supplementary Fig. 6), we observed the same phases at the start and end of the procedure, supporting that these phases are independent of quench speed.

For an electric field strength E = 90 V/mm and average interparticle spacing $r = 1.4\,l$ we calculated that the strength of the dipole-dipole interaction is much smaller than k_BT[4]. This demonstrates that the contribution of dipole-dipole interactions to the stability of the crystal phase can be neglected. The approximately 33% elongation of the BCC lattice along the field direction must therefore be completely due to the anisotropy of the particle and its electrostatic repulsive potential.

We further analyzed the 3D structures by calculating the Voronoi cells around each particle (Supplementary Fig. 8) and found that the rotator phase near dynamical arrest had on average 14 nearest neighbors and Voronoi faces with on average 5 edges, representing the number of particles surrounding a near-neighbor bond. Interestingly, these two distributions are almost identical to the distributions of a glass consisting of hard spheres[17] or spheres with a long-range repulsive potential[27]. We further conclude that this phase transition occurs with minimal particle rearrangements, since the number of nearest neighbors remained constant during the crystallization and melting process. Finally, we determined the distribution of the Voronoi cell volumes (Supplementary Fig. 8e). Using the hard-core particle dimensions (as measured with TEM), both averaged values for the glass and the crystal correspond to a volume fraction of $\phi = 0.017$. This value is higher than the range of volume fractions where a plastic-crystal phase was found in earlier work[4].

Discussion

We demonstrated that when the volume fraction of a suspension of long-ranged repulsive silica rods is increased above a critical value

(ϕ ~0.015), the system failed to crystallize into a plastic (or rotator) crystal phase. Instead, a rotator glass-like phase was found. Particles lacked long-ranged positional order and translational motion slowed down dramatically, whereas rotational motion remained almost free, which is a remarkable demonstration of the decoupling of the glass transitions of the positional and rotational degrees of freedom. Interestingly, this plastic glassy phase could be switched reversibly to a fully ordered crystal when a high-frequency AC electric field was used to restrict particle rotations. Upon decreasing the field strength again, strong hysteresis and a metastable plastic crystal phase were found. When the field strength dropped below a critical value, the crystalline lattice became unstable, and completely returned to its original rotator phase with translational motions near dynamical arrest. We speculate that the effective orientational and time-averaged interactions act similarly as a polydisperse set of particles in destabilizing the crystal with respect to a positional glass forming phase. Using free-energy calculations, we additionally show a thermodynamic origin of such a re-entrant disordered phase for soft rods interacting with simplified interactions but with the same competing tendencies. For the same reasons, again we find that a disordered rotator phase forms due the effective interparticle interactions becoming more anisotropic and effectively polydisperse at higher volume fractions. It is interesting to note that the transitions we observed are similar to the phases predicted by Schilling and Scheidsteger using MCT[28]. Specifically, they predicted that linear rigid molecules could exhibit a phase where the translational degrees of freedom are frozen in but the orientational degrees of freedom remain ergodic, which at high enough packing fractions both become non-ergodic. In contrast, it is also intriguing to report that recently a study on anisotropic colloidal particles has reported a "counterpart" of the rotator glass-former found in our present study that the authors termed a "liquid glass"[29]. In this phase rotations are frozen while translations are fluid, the opposite with respect to the rotational and translational degrees of freedom of the rotator glassy phase. This finding together with our work makes clear that our understanding of the interplay between rotational and translational degrees of freedom for strongly interacting particles or molecular systems is still far from complete. We strongly suspect that similar rotator glassy phases described in this work can also be found for anisotropic rod-like nanoparticles with soft interactions (e.g., polymer like ligands, and/or charged nanorods), and that perhaps for such phases also could appear in molecular systems if repulsions are sufficiently long-ranged. We are certain that knowing that positionally disordered glass-like phases can be equilibrium structures will allow for new theoretical approaches that can be applied to describe this class of glass-formers. The possibility to further study these systems quantitatively on single particle level will also allow further insights in the intricate coupling of rotational and translational degrees of freedom in phase transitions.

Methods

Particle synthesis

Fluorescent silica rod-like particles were synthesized as described in ref. 22. The particles were dyed using fluorescein isothiocyanate (FITC, isomer I, 90%, Sigma-Aldrich). The particles consisted of a three layered structure: a non-fluorescent core, an FITC labeled shell (*ca*. 40 nm) and a non-fluorescent outer shell (*ca*. 100 nm). In the second step, we modified the silica rods with octadecyltrimethoxysilane (OTMOS, 90%, Sigma-Aldrich) by an ultrasonic-assisted coating procedure. In brief, a solution of OTMOS, butylamine (BA, 99.5%, Sigma-Aldrich) and toluene (1:1:10 v/v/v) was prepared, and then 10 wt% of silica rods, that had been dried under nitrogen flow, were added to this solution. The suspension was sonicated at 30–55 °C for 4 h (Branson 2250). Afterwards, the colloidal rods were washed in turn with toluene, cyclohexane and cyclohexylchloride (CHC, >98%, Merck). Finally, the colloidal rods were dispersed in deionized CHC for further use. The particles had an end-to-end length $l = 2.29\ \mu$m ($\delta = 6.0\%$), diameter $d = 600$ nm ($\delta = 6.5\%$), and aspect ratio $l/d = 3.8$. Here, l and d are the mean length and diameter and δ is the polydispersity (standard deviation divided by the mean). A second silica rod system was used without OTMOS modification, which had an average end-to-end length $l = 2.6\ \mu$m (polydispersity $\delta = 9\%$), diameter $d = 630$ nm (polydispersity $\delta = 6\%$) and aspect ratio $l/d = 4.1$.

Sample preparation and Electric field setup

The particles were suspended in cyclohexyl chloride (CHC). The as received CHC (conductivity ≫1.000 pS/cm) was deionized by using molecular sieves (0.4 nm, Aldrich) and activated aluminum oxide (Aldrich). After purification, the CHC had a conductivity as low as 5–10 pS/cm. In this solvent, the particles acquired a negative charge (surface potential −70 mV) and a Debye screening length κ^{-1} ~ 5 μm.

The Debye screening length κ^{-1}, which is given by:

$$\kappa^{-1} = \sqrt{\frac{\epsilon_r \epsilon_0 k_B T}{2 N_A I e^2}}, \tag{1}$$

with ϵ_r the dielectric constant of the solvent, ϵ_0 the permittivity of vacuum, N_A the Avogadro constant, I the concentration of ions in the suspension and e the elementary charge.

The sample was concentrated to a volume fraction ϕ ~0.02 by either sedimentation under gravity or by centrifugation with a maximum of 60 *g*. Rectangular fused quartz capillaries (0.1 × 2 mm^2 and 0.2 × 2 mm^2, VitroCom, UK) were used as sample cells. Electrodes consisting of a 3 nm layer of Cr and a 6–10 nm layer of Au were sputter-coated on two opposing outer surfaces of these capillaries. Thermocouple alloy wires (diameter 50 μm, Goodfellow) were connected to the electrodes with silverpaint (SPI-paint). The ends of the wires were wrapped around standard electronic wires that in turn were connected to the electrical set-up. We used a function generator (Agilent 33120A) to generate a sinusoidal signal with a frequency of 1 MHz and an amplitude of 2.0 V (peak-to-peak). This signal was sent to the sample via a wide band amplifier (Krohn-Hite, 7602M) used to vary the field strength in the sample. The field strength was measured with a digital phosphor oscilloscope (Tektronix TDS3052). We applied a high frequency AC field to prevent polarization of the electric double layer of the particles. After filling the capillaries, they were fixed on a glass slide and sealed with UV-cured glue (Norland, No. 68).

Electric field calculation

Because the electrodes were on the outside of the capillaries, there were three layers of material between the two electrodes. In this case, the field strength is given by[5]

$$E = \frac{V}{\epsilon_0}\left(\frac{\epsilon_1\epsilon_2\epsilon_3}{d_1\epsilon_2\epsilon_3 + d_2\epsilon_1\epsilon_3 + d_3\epsilon_1\epsilon_2}\right), \tag{2}$$

with V the applied voltage, ϵ_0 the dielectric constant of the sample, $\epsilon_{1,-3}$ the dielectric constant of layers 1-3 and d_{1-3} the thickness of layers 1-3. In our experiments, layer 1 and 3 are the glass capillary walls, (thickness d ~0.1 mm and $\epsilon = 3.5$) and layer 2 is (primarily) the solvent CHC (thickness d ~0.1 mm and $\epsilon = 7.6$). The field strength is thus given by $E = 1.9 \times 10^{-3}\ V$ (V/μm). All field strengths in this chapter are given in units V_{RMS}/μm.

In the stepped electric field experiment, we increased the electric field strength in steps of 22.5 V/mm. The duration of each step was 2.8 min and the time interval between measurements was 4 min.

Confocal microscopy measurements

Particles were imaged using a confocal microscope (Leica SP8) equipped with a fast 12 kHz resonant scanner and a GaAsP hybrid detector (Leica HyD™). Images with 8-bit pixel-depth were acquired

using a white light laser with a selected wavelength of 488 nm. A confocal glycerol immersion objective 63x/1.3 (Leica) was used, which is optimized for refractive index n_D = 1.47. To avoid hydrodynamic interactions with the wall, particles were imaged at least 20 μm deep into the sample. To investigate the 3D structure of the suspensions, data stacks were recorded with typical dimensions of 512 × 256 × 120 pixels^3 with voxel size 160 × 160 × 321 nm^3, corresponding to 82 × 41 × 39 μm^3, which were recorded with a frame-rate of 0.3 fps. To track the 3D particle motion, data-stacks were acquired with typical dimensions of 512 × 65 × 25 pixels^3 with voxel size 160 × 160 × 321 nm^3, corresponding to a volume of 82 × 10 × 8 μm^3. The frame-rate for recording these 3D volumes was typically 4 fps. 2D confocal microscopy images had dimensions of 512 × 512 pixels^2 and pixel size of 150 × 150 nm^2, corresponding to typically 75 × 75 μm^2. The 2D images were recorded with a frame-rate of 2–20 fps.

Analysis of static structure

Radial distribution function. To determine the average static structure in our samples, we calculated the radial distribution function $g(r)$. For a given particle, this function describes the probability of finding another particle a distance r away and is given by

$$g(r) = \frac{1}{\rho^2}\langle \sum_{i=1}^{N}\sum_{j\neq i}^{N} \delta(\mathbf{r}_i)\delta(\mathbf{r}_j - \mathbf{r})\rangle, \tag{3}$$

with δ the Dirac delta function, ρ the bulk number density and the angular brackets denoting an ensemble average. N is the total number of particles in the system. The distribution is normalized such that $g(r \to \infty) = 1$.

Nematic order parameter. To quantify the 3D orientational order we calculated the 3D nematic order parameter defined by

$$S_{3D} = \frac{3}{2}\langle \cos^2\theta\rangle - \frac{1}{2}, \tag{4}$$

with θ the angle between the main axis of the rod $\hat{\mathbf{u}}$ and the nematic director $\hat{\mathbf{n}}$. We find S_{3D} and $\hat{\mathbf{n}}$ by calculating the largest eigenvalue and corresponding eigenvector of the standard 3 × 3 nematic order parameter tensor

$$Q^{3D}_{\alpha\beta} = \frac{1}{N}\sum_{i=1}^{N}\left(\frac{3\,u_{i\alpha}u_{i\beta} - \delta_{\alpha\beta}}{2}\right), \tag{5}$$

with $u_{i\alpha}$ the α-component of the unit vector pointing along the main axis of particle i and $\alpha = x, y, z$.

Hexagonal bond order parameter. To quantify the 2D positional order we used the local hexagonal bond-orientational order parameter ψ_{6_k} given by

$$\psi_{6_k} = \frac{1}{n_c(k)}\sum_{j=1}^{n_c(k)} \exp(i6\theta(\mathbf{r}_{jk})), \tag{6}$$

with $n_c(k)$ the number of neighbors of particle k (which is taken to be the number of particles that are within a certain cut-off distance r_c of the particle), $\mathbf{r}_{jk}$ the vector connecting particle k and its neighbor j, $\theta(\mathbf{r}_{jk})$ the angle between $\mathbf{r}_{jk}$ and an arbitrary reference axis and i in the exponent the imaginary unit. In a perfect hexagonal layer, the angles $\theta(\mathbf{r}_{jk})$ are multiples of 60° and $|\psi_{6_k}| = 1$.

Voronoi cell construction. The Voronoi cell of a particle contains all the points in space that are closer to the particle than to any other particle in the system. For monodisperse particles these cells consist of flat faces and straight edges, called polyhedra. We used a publicly available Voronoi software library (Voro++[30]) to calculate 3D Voronoi cells, the number of Voronoi nearest neigbours, the number of edges per Voronoi face and the average Voronoi cell volume.

Analysis of particle dynamics

To study the particle dynamics, we applied our particle-fitting algorithm to time-series of 3D confocal microscopy data-stacks, as described in detail in ref. 21. We calculated the mean squared displacement (MSD) given by

$$\Delta\mathbf{r}^2(t) \equiv \langle|\mathbf{r}(t) - \mathbf{r}(0)|^2\rangle, \tag{7}$$

which we fitted to the expression

$$\Delta\mathbf{r}^2(t) = 6\,D_t\,t + 6\,\epsilon_t^2, \tag{8}$$

with D_t the rotationally averaged translational diffusion coefficient and ϵ_t the error in measurement of each of the coordinates of the particle[31]. For the highest volume fractions, we could not reach the region where the long-term translational dynamics become diffusive again, i.e., $\langle\Delta r^2(t)\rangle \sim t$. For the mean squared angular displacement (MSAD) we used the expression[32,33]

$$\langle\Delta\hat{\mathbf{u}}^2(t)\rangle = 2[1 - (1 - \epsilon_r^2)\exp(-2D_r t)], \tag{9}$$

with D_r the average rotational diffusion coefficient and ϵ_r the measurement error in the determination of $\hat{\mathbf{u}}(t)$. To further quantify the rotational motion of the particles, we also calculated the orientation auto-correlation function

$$C(t) = \langle\hat{\mathbf{u}}(0)\cdot\hat{\mathbf{u}}(t)\rangle, \tag{10}$$

which we fitted with a stretched exponential function, given by

$$C(t) = (1 - \epsilon_r^2)\exp(-(t/\tau_r)^\beta), \tag{11}$$

with ϵ_r the measurement error in the determination of the direction of the main axis of the rods, τ_r the typical orientation relaxation time and β the Kohlrausch exponent. At infinite dilution we have $\beta = 1$ and $\tau_r = 1/(2\,D_r)$ with D_r the rotational diffusion coefficient[32]. For the analysis of the translational correlations, we calculated the self-intermediate scattering function, given by

$$F_s(q,t) = \langle\frac{1}{N}\sum_{j=1}^{N}\exp[i\mathbf{q}\cdot(\mathbf{r}_j(t) - \mathbf{r}_j(0))]\rangle, \tag{12}$$

with $\mathbf{q}$ the wavevector with magnitude equal to the first peak of the radial distribution function $g(r)$, and $\mathbf{r}_j(t)$ the three dimensional position vector of particle j at time t and the brackets denoting an ensemble average. $F_s(q, t)$ was fitted with a similar stretched exponential as we used for the orientational correlation function

$$F_s(t) = a\exp(-(t/\tau_t)^\beta), \tag{13}$$

with a a pre-factor that includes the error in the determination of the position of the rod, τ_t the typical translational relaxation time and β the Kohlrausch exponent.

Yukawa segment model

We employed the Yukawa segment model[24], in which a charged rod is divided into in n segments of equally distributed point charges along the rod axis. The interactions between two rods is then given by the

sum of the interactions between the segments:

$$\beta U_{ij}(\mathbf{r}_i - \mathbf{r}_j, \mathbf{u}_i, \mathbf{u}_j) = \beta\Gamma \sum_{a,b=1}^{n} \frac{\exp[-\kappa r_{ij}^{ab}]}{r_{ij}^{ab}}, \quad (14)$$

with κ the screening length, $\beta\Gamma$ the energy scale between two segments, and $\beta = 1/k_BT$, where k_B is the Boltzmann constant and T is the temperature, and

$$r_{ij}^{ab} = |\mathbf{r}_i - \mathbf{r}_j + \mathbf{u}_i d_n(2a - 1 - n)/2 - \mathbf{u}_j d_n(2b - 1 - n)/2|, \quad (15)$$

the distance between segment a of rod i and segment b of rod j, where d_n denotes the distance between neighboring segments

$$d_n = \frac{l}{\sqrt{(n+1)(n-1)}}. \quad (16)$$

Since the system we investigated is highly charged, the rods never came into close contact and we can safely omit the hard-core interactions in our simulations.

Free energy calculations

We determined the equilibrium phase behavior of our rod-like particles by calculating the Helmholtz free energy of both the fluid phase and the BCC crystal phase. To this end, we first calculated a "reference" free energy of both the fluid and crystal phase at a single density using the Widom insertion method and Frenkel-Ladd method, respectively[34]. Subsequently, the Helmholtz free energy of both phases was calculated for a range of densities and energy scales (temperatures) using thermodynamic integration of the equation of state and temperature-dependent average potential energy, as calculated using Monte Carlo simulations in the *NVT*-ensemble. In these calculations, we have restricted ourselves to densities and energy scales up to $\rho l^3 \approx 0.65$ and $\beta\Gamma \approx 68$, respectively. Note that in the simulations we have chosen to use a shorter ranged interaction than in the experiments. This choice has ensured that the system is fast enough for the simulations involved with the thermodynamic integration to equilibrate. This, however, also means that the system shows a re-entrant fluid, not a re-entrant glass.

Brownian dynamics simulations

We performed Brownian dynamics simulations of the Yukawa segment model following ref. 26. Here, we have mapped the self-diffusion coefficients to the experimental system by matching the ratios between the rotational and the two translational diffusion coefficients. We measured time in units of the translational diffusion at infinite dilution $\tau_B = l^2/D_t^0$.

Data availability

The data that support the findings of this study are available in a data package on Zenodo https://doi.org/10.5281/zenodo.18482452

References

1. Chaikin, P. M. & Lubensky, T. C. *Principles of Condensed Matter Physics* (Cambridge University Press, Cambridge, England, 1995).
2. Timmermans, J. Plastic crystals: a historical overview. *J. Phys. Chem. Solids* **18**, 1–8 (1961).
3. Lekkerkerker, H. N. W. & Vroege, G. J. Liquid crystal phase transitions in suspensions of mineral colloids: new life from old roots. *Philos. Trans. R. Soc. A* **371**, 20120263 (2013).
4. Liu, B. et al. Switching plastic crystals of colloidal rods with electric fields. *Nat. Commun.* **5**, 3092 (2014).
5. Kuijk, A., Byelov, D. V., Petukhov, A. V., van Blaaderen, A. & Imhof, A. Phase behavior of colloidal silica rods. *Faraday Discuss.* **159**, 181–199 (2012).
6. Schadt, M. Liquid crystal materials and liquid crystal displays. *Annu. Rev. Mater. Sci.* **27**, 305–379 (1997).
7. Berthier, L. & Biroli, G. Theoretical perspective on the glass transition and amorphous materials. *Rev. Modern Phys.* **83**, 587–645 (2011).
8. McKenna, G. B. Looking at the glass transition: challenges of extreme time scales and other interesting problems. *Rubber Chem. Technol.* **93**, 79–120 (2020).
9. Weeks, E. R. Introduction to the colloidal glass transition. *ACS Macro Lett.* **6**, 27–34 (2017).
10. Hunter, G. L. & Weeks, E. R. The physics of the colloidal glass transition. *Rep. Prog. Phys.* **75**, 066501 (2012).
11. Gokhale, S., Sood, A. K. & Ganapathy, R. Deconstructing the glass transition through critical experiments on colloids. *Adv. Phys.* **65**, 363–452 (2016).
12. Tanaka, H., Tong, H., Shi, R. & Russo, J. Revealing key structural features hidden in liquids and glasses. *Nat. Rev. Phys.* **1**, 333–348 (2019).
13. Sidebottom, D. L. Connecting glass-forming fragility to network topology. *Front. Mater.* **6**, 1–14 (2019).
14. Janssen, L. M. C. Active glasses. *J. Phys. Condens. Matter* **31**, 1–21 (2019).
15. Angelini, T. E. et al. Glass-like dynamics of collective cell migration. *Proc. Natl. Acad. Sci. USA* **108**, 4714–4719 (2011).
16. Grosser, S. et al. Cell and Nucleus Shape as an Indicator of Tissue Fluidity in Carcinoma. *Phys. Rev. X* **11**, 1–24 (2021).
17. van Blaaderen, A. & Wiltzius, P. Real-space structure of colloidal hard-sphere glasses. *Science* **270**, 1177–1179 (1995).
18. Brambilla, G. et al. Probing the equilibrium dynamics of colloidal hard spheres above the mode-coupling glass transition. *Phys. Rev. Lett.* **102**, 1–4 (2009).
19. Martinez-Veracoechea, F. J., Mladek, B. M., Tkachenko, A. V. & Frenkel, D. Design rule for colloidal crystals of DNA-functionalized particles. *Phys. Rev. Lett.* **107**, 045902 (2011).
20. Smallenburg, F. & Sciortino, F. Liquids more stable than crystals in particles with limited valence and flexible bonds. *Nat. Phys.* **9**, 554–558 (2013).
21. Besseling, T. H. et al. Determination of the positions and orientations of concentrated rod-like colloids from 3D microscopy data. *J. Phys. Condens. Matter* **27**, 194109 (2014).
22. Kuijk, A., van Blaaderen, A. & Imhof, A. Synthesis of monodisperse, rodlike silica colloids with tunable aspect ratio. *J. Am. Chem. Soc.* **133**, 2346–2349 (2011).
23. Kegel, W. K. & van Blaaderen, A. Direct observation of dynamical heterogeneities in colloidal hard-sphere suspensions. *Science* **287**, 290–293 (2000).
24. Schneider, J., Hess, W. & Klein, R. The static structure factor of a dilute system of charged rods in solution. *J. Phys. A Math. Gen.* **18**, 1221 (1985).
25. Royall, C. P. & Williams, S. R. The role of local structure in dynamical arrest. *Phys. Rep.* **560**, 1–75 (2015).
26. Kirchhoff, T., Löwen, H. & Klein, R. Dynamical correlations in suspensions of charged rodlike macromolecules. *Phys. Rev. E* **53**, 5011 (1996).
27. van der Linden, M. N., El Masri, D., Dijkstra, M. & van Blaaderen, A. Expansion of charged colloids after centrifugation: formation and crystallisation of long-range repulsive glasses. *Soft Matter* **9**, 11618 (2013).
28. Schilling, R. & Scheidsteger, T. Mode coupling approach to the ideal glass transition of molecular liquids: linear molecules. *Phys. Rev. E* **56**, 2932 (1997).
29. Roller, J., Laganapan, A., Meijer, J. M., Fuchs, M. & Zumbusch, A. Observation of liquid glass in suspensions of ellipsoidal colloids. *Proc. Natl. Acad. Sci. USA* **118**, e2018072118 (2021).

30. Rycroft, C. H. VORO++: a three-dimensional voronoi cell library in C++. *Chaos* **19**, 041111 (2009).
31. Savin, T. & Doyle, P. S. Static and dynamic errors in particle tracking microrheology. *Biophys. J.* **88**, 623–638 (2005).
32. Dhont, J. K. G. *An Introduction to Dynamics of Colloids* (Elsevier, Amsterdam, 1996).
33. Cheong, F. C. & Grier, D. G. Rotational and translational diffusion of copper oxide nanorods measured with holographic video microscopy. *Opt. Express* **18**, 6555–6562 (2010).
34. Frenkel, D. & Smit, B. *Understanding Molecular Simulation: From Algorithms to Applications* (Elsevier Publishing, Amsterdam, The Netherlands, 2023).

Acknowledgements

Part of the research leading to these results has received funding from the European Research Council under the European Unions Seventh Framework Program (FP/2007-2013)/ERC Grant Agreement no. [291667: HierarSACol] (A.v.B).

Author contributions

A.v.B. initiated the project. A.v.B., A.I. and L.F. supervised the research. T.H.B., A.I. and A.v.B. designed the experiments and T.H.B. performed the experiments. T.H.B. and B.L. performed particle synthesis and B.L. performed preliminary experiments and contributed to the characterization of the phase behavior. B.v.d.M. and L.F. designed the simulations and B.v.d.M. performed the simulations. A.v.B., A.I., T.H.B., B.v.d.M. and L.F. analysed the data and co-wrote the manuscript.

Competing interests

The authors declare no competing interests.

Additional information

Supplementary information The online version contains supplementary material available at https://doi.org/10.1038/s41467-026-70295-5.

Correspondence and requests for materials should be addressed to Thijs Herman Besseling or Alfons van Blaaderen.

Peer review information *Nature Communications* thanks the anonymous reviewer(s) for their contribution to the peer review of this work. A peer review file is available.